Research Article

High-performance planar heterojunction perovskite solar cells: Preserving long charge carrier diffusion lengths and interfacial engineering

Sai Bai[1,§], Zhongwei Wu[2,§], Xiaojing Wu[3], Yizheng Jin[1] (✉), Ni Zhao[3,4], Zhihui Chen[1], Qingqing Mei[1], Xin Wang[1], Zhizhen Ye[1], Tao Song[2], Ruiyuan Liu[2], Shuit-tong Lee[2], and Baoquan Sun[2] (✉)

[1] *State Key Laboratory of Silicon Materials, Cyrus Tang Center for Sensor Materials and Applications, Department of Materials Science and Engineering, and Center for Chemistry of High-Performance and Novel Materials, Zhejiang University, Hangzhou 310027, China*
[2] *Jiangsu Key Laboratory for Carbon-Based Functional Materials & Devices, Institute of Functional Nano & Soft Materials (FUNSOM) and Collaborative Innovation Center of Suzhou Nano Science and Technology, Soochow University, 199 Ren'ai Road, Suzhou 215123, China*
[3] *Department of Electronic Engineering, the Chinese University of Hong Kong, Shatin, New Territories, Hong Kong, China*
[4] *Shenzhen Research Institute, the Chinese University of Hong Kong, Shatin, New Territories, Hong Kong, China*
[§] *Both authors contributed equally to this work.*

ABSTRACT

We demonstrate that charge carrier diffusion lengths of two classes of perovskites, $CH_3NH_3PbI_{3-x}Cl_x$ and $CH_3NH_3PbI_3$, are both highly sensitive to film processing conditions and optimal processing procedures are critical to preserving the long carrier diffusion lengths of the perovskite films. This understanding, together with the improved cathode interface using bilayer-structured electron transporting interlayers of [6,6]-phenyl-C_{61}-butyric acid methyl ester (PCBM)/ZnO, leads to the successful fabrication of highly efficient, stable and reproducible planar heterojunction $CH_3NH_3PbI_{3-x}Cl_x$ solar cells with impressive power-conversion efficiencies (PCEs) up to 15.9%. A 1-square-centimeter device yielding a PCE of 12.3% has been realized, demonstrating that this simple planar structure is promising for large-area devices.

1 Introduction

Solution-processed photovoltaics manufactured by high-throughput printing and coating techniques are attractive for low-cost and large-area solar energy harvesting. For many solution-processed photovoltaics, such as organic solar cells, dye-sensitized solar cells and colloidal quantum dot solar cells, the exciton or

Address correspondence to Yizheng Jin, yizhengjin@zju.edu.cn; Baoquan Sun, bqsun@suda.edu.cn

charge carrier diffusion lengths of the absorber materials are considerably shorter than their absorption lengths [1–5]. Hence complex device structures with highly nanostructured or mesostructured heterojunctions are required to overcome this imbalance and achieve high power-conversion efficiencies (PCEs) [5–7].

Recently solution-processed methylammonium lead halide perovskites, with absorption depths between 100 and 200 nm depending on the wavelengths of the incident light, were identified as promising absorbers for high-performance solar cells [8–25]. Stranks and coworkers conducted a time-resolved photoluminescence (PL) quenching experiment on the mixed halide perovskite, $CH_3NH_3PbI_{3-x}Cl_x$. By fitting the data to a diffusion model, they showed that the diffusion lengths for both electrons and holes in the material are greater than 1 μm [12]. Xing et al. [13] identified balanced long-range electron–hole diffusion lengths of at least 100 nm for $CH_3NH_3PbI_3$ by a similar method. The remarkably long charge carrier diffusion length is a key factor in simultaneously allowing sufficient light absorption and efficient charge transport/extraction to achieve high photocurrents. Therefore the perovskites are ideal for thin film photovoltaics, as demonstrated by a number of recent publications reporting that devices with simple planar heterojunction structures exhibited high PCEs ranging from 3.9% to more than 15% [12, 16, 23–33].

Herein, we show that the charge carrier diffusion lengths of methylammonium lead halide perovskites are largely controlled by processing conditions. By fitting the PL decay data to the diffusion model, we find that annealing the $CH_3NH_3PbI_{3-x}Cl_x$ film at 150 °C for 1 min leads to decrease of electron and hole diffusion lengths from 1,133 ± 113 and 594 ± 59 nm to 297 ± 30 and 220 ± 20 nm, respectively. The electron and hole diffusion lengths for the $CH_3NH_3PbI_3$ films from sequential deposition can reach 807 ± 30 and 813 ± 30 nm, respectively, much longer than the lower limit of ~100 nm estimated from the $CH_3NH_3PbI_3$ films prepared by different processing conditions [12, 13]. These results demonstrate that optimal processing procedures are required to preserve the long charge carrier diffusion lengths of perovskite films. Based on this understanding, we succeeded in designing a high-performance planar heterojunction solar cell structure that can be low-temperature processed to avoid degradation of the carrier diffusion lengths of the perovskite films. Furthermore a ZnO nanocrystal layer, fabricated from solution by annealing-free processing, is introduced as an electron-transporting and hole-blocking interlayer to improve the cathode interface. The optimized device structure and fabrication procedures yield highly efficient, stable and reproducible $CH_3NH_3PbI_{3-x}Cl_x$ solar cells with PCEs up to 15.9%.

2   Results and discussion

The mixed halide perovskite, $CH_3NH_3PbI_{3-x}Cl_x$, is used as a model system to investigate the effects of post-deposition annealing treatment on the charge carrier diffusion lengths. The methylammonium lead halide perovskites are known to be moisture sensitive [34, 35]. Therefore all fabrication procedures for the $CH_3NH_3PbI_{3-x}Cl_x$ films were carried out in a nitrogen filled glovebox with moisture level below 1 ppm to ensure the consistency of material properties. The "pristine" $CH_3NH_3PbI_{3-x}Cl_x$ films (Fig. S1 in the in the Electronic Supplementary Material (ESM)) of 200 ± 20 nm in thickness, were obtained by spin-coating the precursor solutions onto oxygen plasma-cleaned glass substrates, followed by annealing at 95 °C for ~15 min. To study the temperature effect, four sets of samples were prepared by annealing the pristine $CH_3NH_3PbI_{3-x}Cl_x$ films at 80 °C for 10 min, at 100 °C for 10 min, at 130 °C for 3 min and at 150 °C for 1 min, respectively. Figure S2(a) (in the ESM) shows the typical absorption and PL spectra of the pristine perovskite films, confirming that the PL corresponds to the band edge transition. The PL lifetime (the time taken for the PL to fall to 1/e of its initial intensity) for the pristine film, measured at the peak emission of 775 ± 5 nm by the time-correlated single-photon counting (TCSPC) technique, is 205 ns (Fig. 1(a)). Upon further annealing, the PL intensity measured under identical conditions starts to decrease (Fig. S2(b) in the ESM). At the same time the PL lifetimes of the annealed films are decreased to 171, 127, 59 and 30 ns, respectively, following the increase of the post-deposition annealing temperature (Fig. 1(a)).
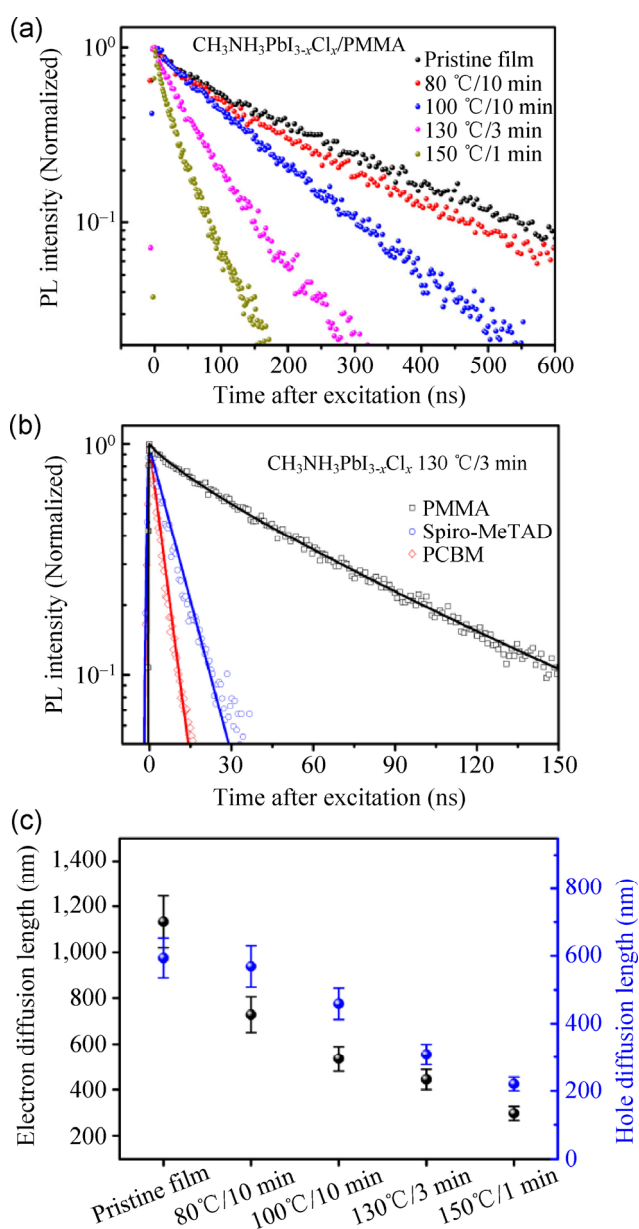
Figure 1 Effects of post-deposition annealing treatment on PL lifetime and charge carrier diffusion lengths of the $CH_3NH_3PbI_{3-x}Cl_x$ films. (a) Time-resolved PL decay transients measured at the peak emission of the perovskite films (covered with PMMA). (b) Time-resolved PL decay transient data (open symbols) of the perovskite films that were treated at 130 °C for 3 min, including the perovskite films covered with PMMA, PCBM quencher or spiro-OMeTAD quencher layers, along with PL decay fittings (solid lines), i.e. the stretched exponential fitting to the perovskite/PMMA sample and the fitting to the quenching samples by using the diffusion model described in the ESM. (c) The electron and hole diffusion lengths of the $CH_3NH_3PbI_{3-x}Cl_x$ films. The errors quoted arise predominantly from thickness variations of the films.

Time-resolved PL quenching experiments were conducted on these samples by using 2,2′,7,7′-tetrakis(*N*,*N*′-di-p-methoxyphenylamine)-9,9′-spirobi fluorene (spiro-OMeTAD) as the hole-quenching layer or [6,6]-phenyl-C_{61}-butyric acid methyl ester (PCBM) as the electron-quenching layer (Fig. 1(b)). Based on the PL decay data, charge carrier diffusion lengths of the perovskite films were extracted following the method described by Stranks and coworkers [12] (details provided in the ESM). The results are summarized in Fig. 1(c) and Table 1. Due to the approximations and assumptions of the diffusion model, e.g. 100% quenching efficiency at the extraction-layer interface, these values may be underestimated and should be considered as the lower limits. The electron and hole diffusion lengths for the pristine films are 1,133 ± 113 and 594 ± 59 nm, respectively. In contrast, after annealing at 150 °C for 1 min, the electron and hole diffusion lengths are found to be 297 ± 30 and 220 ± 20 nm, respectively. The electron and hole diffusion lengths are relatively unbalanced in our mixed halide perovskites as compared to those reported by Stranks and coworkers [12]. We suggest that the hybrid perovskite films may exhibit very different charge carrier diffusion lengths since many factors, including film compositions, film-deposition methods, and processing conditions may influence the electronic structures. For example, in a recent report, Eperon and coworkers [33] showed that the hole diffusion length for the formamidinium lead trihalide perovskite films is 813 ± 72 nm, much longer than the electron diffusion length, 177 ± 20 nm.

Further control experiments on the $CH_3NH_3PbI_{3-x}Cl_x$ films show that for a given post-deposition annealing temperature, extending the annealing time also leads to decrease of both PL lifetime and charge carrier diffusion lengths (Fig. S3(a) in the ESM). For example, the PL lifetime and the electron and hole diffusion lengths for the films annealed at 130 °C for 5 min are 45 ns and 411 ± 41 and 249 ± 25 nm, respectively, shorter than those for the films annealed at 130 °C for 3 min (Fig. S3(a) in the ESM). Although we could not obtain the exact values for the films that were annealed at 150 °C for 10 min due to the weak emission properties and the very short PL lifetime of ~2 ns (Fig. S3(b) in the ESM), we believe that both the

Table 1 Summary of PL lifetime (τ_e) and diffusion lengths (L_D) of the perovskite films. The errors quoted arise from the film thickness variations, which are ± 20 nm for the $CH_3NH_3PbI_{3-x}Cl_x$ films and ± 10 nm for the sequential deposited $CH_3NH_3PbI_3$ films

Perovskite		τ_e (ns)	Species	L_D (nm)
$CH_3NH_3PbI_{3-x}Cl_x$	Pristine film	205	Electrons	1,133 ± 113
			Holes	594 ± 59
$CH_3NH_3PbI_{3-x}Cl_x$ (Post-deposition annealing treatment)	80 °C for 10 min	171	Electrons	729 ± 77
			Holes	569 ± 61
	100 °C for 10 min	127	Electrons	535 ± 54
			Holes	459 ± 46
	130 °C for 3 min	59	Electrons	444 ± 44
			Holes	308 ± 31
	150 °C for 1 min	30	Electrons	297 ± 30
			Holes	220 ± 20
$CH_3NH_3PbI_3$	Sequential deposition	16	Electrons	807 ± 30
			Holes	813 ± 30

electron and hole diffusion lengths should be no longer than 100 nm. These results indicate that post-deposition annealing temperatures of above 100 °C are not favorable in terms of preserving the long charge carrier diffusion lengths of the perovskite films. These results also imply that for the processing of perovskite films by one-step annealing of precursors, once the perovskite structures are formed, elongating the thermal treatment at high temperatures may deteriorate the carrier diffusion lengths of the films.

X-ray diffraction (XRD) and scanning electron microscopy (SEM) measurements were performed to explore the origin of the decreased carrier diffusion lengths in the relatively high temperature treated samples. We investigate the pristine $CH_3NH_3PbI_{3-x}Cl_x$ film and four other films annealed at 80 °C, 100 °C, 130 °C and 150 °C for 10 min, respectively. XRD results reveal that the higher is the annealing temperature, the stronger is the intensity of the peak at 12.6°. This peak corresponds to the PbI_2 phase (Fig. 2(a)). This trend is consistent with the SEM images (Figs. 2(b)–2(e) and Fig. S4 in the ESM) showing that small domains grow on the surfaces of perovskite films upon annealing at temperatures above 100 °C. We therefore suggest that annealing the pristine films at temperatures above 100 °C may result in the partial decomposition of the perovskites, generating PbI_2 domains in the films. Therefore the nanoscale three-dimensional structure

of the hybrid perovskite deteriorated, leading to structural defects that significantly quench the PL, shorten the PL lifetimes, and reduce the charge carrier diffusion lengths. In the course of preparing this manuscript, we noticed a very recent report by Dualeh et al [36]. on solar cells using $CH_3NH_3PbI_3$ as the sensitizer. They found that increasing the film-formation temperature to over 100 °C is accompanied by an increased amount of PbI_2 content in the film, which is coincident with our post-deposition annealing results.

Based on the above findings, we fabricated thin-film planar heterojunction $CH_3NH_3PbI_{3-x}Cl_x$ solar cells by low-temperature (< 100 °C) processing to preserve the long charge carrier diffusion lengths of the perovskite absorbers. We also modified the cathode interface and developed a photovoltaic structure of indium tin oxide (ITO)/poly(3,4-ethylenedioxythiophene):poly(styrene sulfonate) (PEDOT:PSS)/perovskite/PCBM/ZnO nano-crystal/Al (Fig. 3(a)). A typical cross-section SEM image of the devices is shown in Fig. 3(b). In this device structure, thick $CH_3NH_3PbI_{3-x}Cl_x$ layers (~400 nm) are used to maximize photon absorption. PCBM acts as an excellent electron-extracting layer for the perovskite absorbers, as demonstrated by several previous studies [25, 26, 28–30, 32]. As discussed below, introducing additional layers of ZnO nanocrystals significantly improves the cathode interface. These concerted
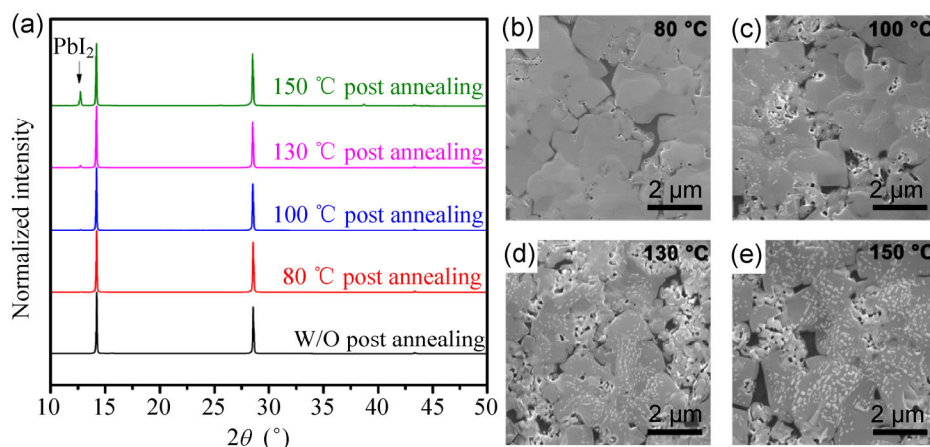
Figure 2 Effects of post-deposition annealing treatment (10 min) on the structural and morphological properties of the $CH_3NH_3PbI_{3-x}Cl_x$ films. (a) XRD profiles of the $CH_3NH_3PbI_{3-x}Cl_x$ films. (b)–(e) SEM images showing the top-views of the $CH_3NH_3PbI_{3-x}Cl_x$ film in (a) treated at 80 °C (b), 100 °C (c), 130 °C (d) and 150 °C (e). Larger magnification SEM images of the perovskite films with or without post-deposition annealing treatment are shown in Fig. S4 (in the ESM).
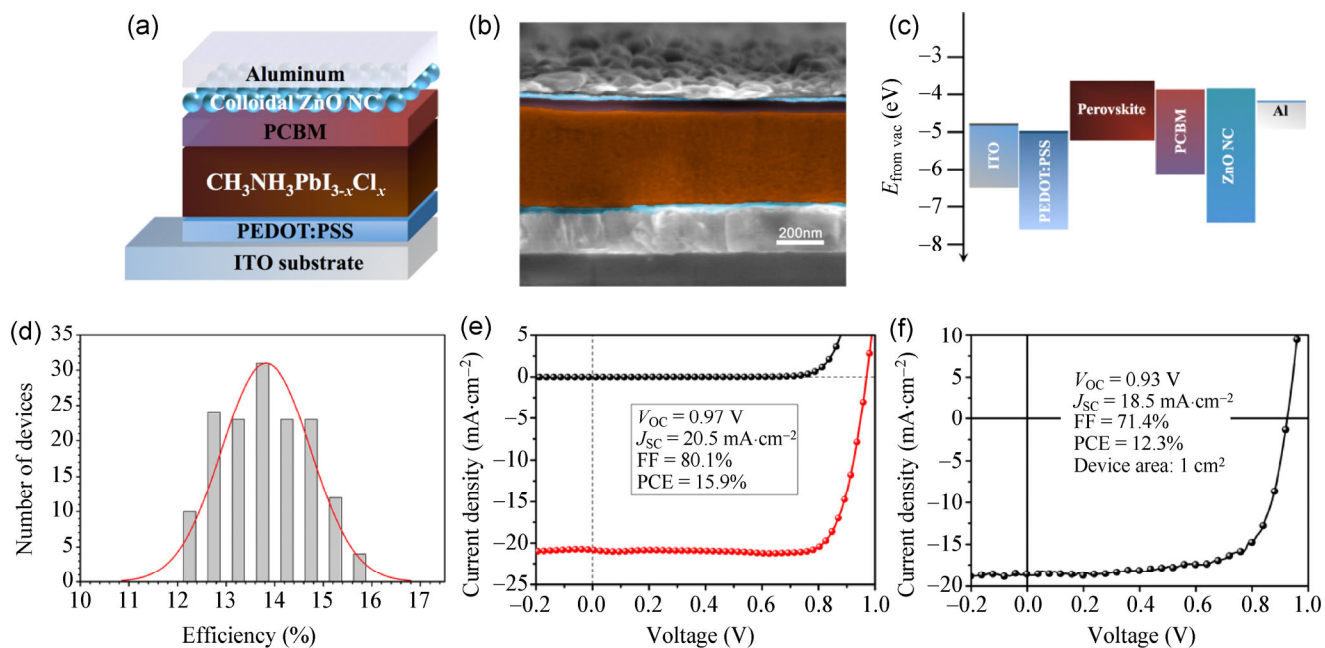

Figure 3 Device structure and performance of our $CH_3NH_3PbI_{3-x}Cl_x$ solar cells. (a) Schematic structure. (b) A typical cross-sectional SEM image showing the device configuration. The layers are tinted by different colors. (c) Energy level (relative to vacuum) diagram of the various components used in our devices. The ordinate refers to the electron energy relative to the vacuum level. (d) A histogram of PCEs measured from 150 devices. The histograms of other electrical parameters are shown in Fig. S5 (in the ESM). (e) J–V curves of our champion device under AM 1.5G illumination of 100 mW·cm^{-2} (red line) and in the dark (black line). (f) Light J–V curve of a large-area (1 cm^2) device.

efforts lead to highly efficient and reproducible solar cells with excellent ambient stability. As shown by the histograms of device parameters for 150 solar cells (Fig. 3(d) and Fig. S5 in the ESM), the high average PCE of 13.8% and low relative standard deviation in PCEs of 6.6% are both encouraging. Notably all the

devices were tested without any encapsulation under ambient conditions. While no systematic investigation has been undertaken in the present work, our devices were found to be stable under ambient conditions (Fig. S6 in the ESM). For comparison, the devices without ZnO nanocrystal interlayers exhibit poor

stability. The efficiency degraded completely after 30 min of air exposure (Fig. S6 in the ESM). The champion device exhibits a remarkable fill factor (FF) of 0.80 and a PCE of 15.9% (Fig. 3(e)). Integrating the overlap of the external quantum efficiency (EQE) spectrum (Fig. S7(a) in the ESM) with the AM 1.5G solar photon flux generates a current density of 19.2 mA·cm^{-2}, which is close to the measured short-circuit photocurrent (J_{SC}) density of 20.5 mA·cm^{-2}. The internal quantum efficiency (IQE) spectrum, derived from the EQE and light harvesting efficiency (LHE) spectra (Fig. S7 in the ESM), indicates near-unity quantum yield for the generation and collection of charge carriers. The large J_{SC} and the high photon-to-current conversion efficiency reflect the combination of maximized optical absorption, excellent charge transport, and minimized interfacial losses of our devices. The average PCE of 13.8% and the champion PCE of 15.9% make our perovskite devices one of the best-performing solution-processed solar cells ever reported to date. Note that an anomalous hysteresis is often observed in the current–voltage measurements of the perovskite solar cells, but the origin of this hysteresis is not understood [37]. In this regard, we also measured the hysteresis behavior of our devices. As shown in Fig. S8 (in the ESM), the PCE for the scan from the forward bias to short-circuit is about 1% higher than that of the scan from the short-circuit to forward bias.

We highlight that the introduction of an additional ZnO nanocrystal interlayer between the PCBM and Al electrode is critical in terms of improving the hole-blocking properties of the cathode contacts, preventing the direct contact of the electrodes and the perovskite layers, and enhancing the ambient stability of the devices. The ZnO interlayer dramatically improves the hole-blocking capability due to its deep valence band level (Fig. 3(c)). The enhanced charge selectivity of the cathode contacts is confirmed by the suppressed dark currents of the devices. As shown in Fig. S9 (in the ESM), the reverse saturation dark current of our device is about one order of magnitude lower than that of the device without the ZnO nanocrystal interlayer. We found that for devices with thick perovskite layers (~400 nm), a single PCBM layer is often insufficient to achieve full coverage and com-

pletely isolate the perovskite semiconductor from the top electrodes (Fig. S10 in the ESM). As shown by our control studies, devices with the top electrode of Al directly contacting the perovskite layer exhibit very small PCEs (Fig. S11 in the ESM). Accordingly, the devices without the ZnO interlayers exhibit a lower average PCE of 7.5% and a larger relative standard deviation in PCE, 28.6% (Fig. S12 in the ESM). The introduction of additional ZnO interlayers solves this contact problem and significantly improves the device reproducibility. Furthermore, the ZnO interlayer prevents metal diffusion into the PCBM layer, enhancing ambient stability of our devices [38–40]. It is worth mentioning that to achieve the device structure that yields high photovoltaic performance we select ethanol to disperse ZnO nanoparticles (Fig. S13 in the ESM) such that (1) the ZnO solution does not dissolve the underlying PCBM layer and (2) the ZnO nanoparticles can spontaneously form close-packed films upon solvent evaporation. In this way, the ZnO nanocrystal films are processed at room temperature while yielding good electron transport properties without any additional sintering procedures [41, 42]. This advantage is important in terms of preserving the long charge carrier diffusion lengths of the perovskite layers. As shown in Fig. S14 and Table S1 in the ESM, our comparative studies show that the device with longest charge carrier diffusion lengths has the best PCE. The high-temperature annealed perovskite films exhibit shorter charge carrier diffusion lengths, and hence result in lower PCEs.

The performance of large-area devices is very important to evaluate the large-scale module application in future. It is rather challenging to achieve a high-quality film with a relative large area (> 1 cm^2) for most solution-processed devices [43]. For perovskite solar cells, much less attention has been paid to large-area device performance in comparison to achieving the highest PCE value. Here, we demonstrate a PCE of 12.3% for 1-cm^2 devices (Fig. 3(f), which is the best PCE value for devices of this size and represents an improvement of ~50% for perovskite solar cells of the same size [25]. The lower FF is one of the main factors in the decrease in PCE, possibly resulting from the inferior conductivity of ITO.

Inspired by the results for the CH$_3$NH$_3$PbI$_{3-x}$Cl$_x$

films, we also explore the charge carrier diffusion lengths of another important methylammonium lead halide perovskite, $CH_3NH_3PbI_3$. Previous studies suggest that the charge carrier diffusion lengths for the $CH_3NH_3PbI_3$ films, which were deposited from precursor solutions by one-step methods, as determined by the diffusion model are ~100 nm [12, 13]. Here we measured the charge carrier diffusion lengths of $CH_3NH_3PbI_3$ films deposited by the sequential deposition approach [14, 24]. As shown in Fig. 4(a), the two-step method results in pin-hole free films with thicknesses of 270 ± 10 nm. The PL lifetime of our $CH_3NH_3PbI_3$ films is determined to be 16 ns. This value is longer than those in previous reports [12, 13], reflecting the excellent quality of the $CH_3NH_3PbI_3$ films formed using the sequential deposition approach. The electron and hole diffusion lengths for our $CH_3NH_3PbI_3$ films are determined to be 807 ± 30 and 813 ± 30 nm, respectively, much longer than the absorption depths of the films (Fig. 4(b) and Table 1). In Stranks's work, the $CH_3NH_3PbI_3$ films were prepared by annealing the spin-coated precursors at 150 °C for 15 min [12]. The relatively high temperature processing may deteriorate the charge carrier diffusion lengths. In the report by Xing et al. [13], very thin films of ~65 nm in thickness were used for measurements. Therefore the carrier lifetime and in consequence the charge diffusion lengths are more susceptible to the non-ideality of the interfaces. These results suggest that the charge carrier diffusion lengths for the $CH_3NH_3PbI_3$

films are also highly sensitive to processing. Our results may explain the high performance of recently reported planar $CH_3NH_3PbI_3$ solar cells with the absorber thicknesses of ~300 nm and PCEs ranging from 12.1% to 15.7% [23–25]. As long as the long charge diffusion lengths can be preserved, the optimal thickness of the $CH_3NH_3PbI_3$ absorber in planar solar cells is not limited to ~100 nm.

3   Conclusions

We have shown that the charge carrier diffusion lengths of the methylammonium lead halide perovskites are highly dependent on the processing conditions. When processed at mild temperatures, both the $CH_3NH_3PbI_{3-x}Cl_x$ and $CH_3NH_3PbI_3$ films can exhibit charge carrier diffusion lengths much greater than the corresponding absorption depths of 100 to 200 nm. Annealing the pristine $CH_3NH_3PbI_{3-x}Cl_x$ films at temperatures above 100 °C leads to partial decomposition of the perovskites and formation of PbI_2, which significantly reduces the charge carrier diffusion lengths. This important finding, together with an improved cathode interface design by integrating interlayers of ZnO nanocrystals, allowed us to fabricate efficient and reproducible solar cells with excellent ambient stability and PCEs as high as 15.9% by low-temperature processing. These advantages have been exploited to achieve a PCE of 12.3% for one-square-centimeter devices. Both PCEs are among
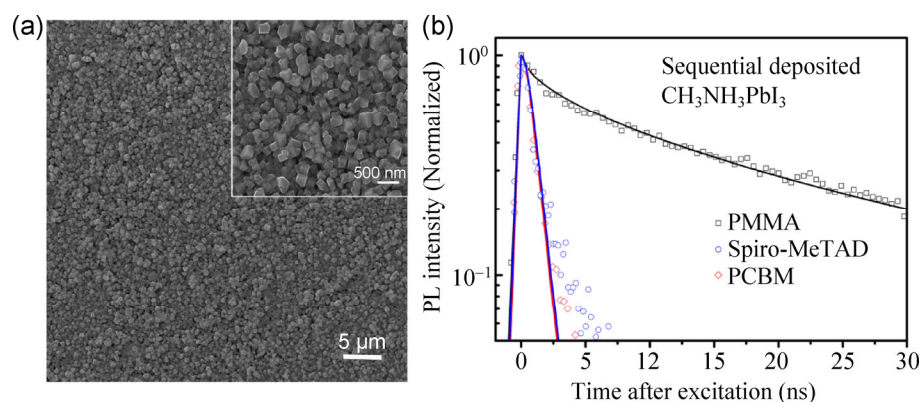

Figure 4 $CH_3NH_3PbI_3$ films obtained by the two-step sequential deposition approach. (a) Top-view SEM images (inset image with higher resolution) showing the pin-hole free feature of the $CH_3NH_3PbI_3$ films. (b) Time-resolved PL decay transient data (open symbols) and the fitting (solid lines) data to the $CH_3NH_3PbI_3$ with and without the quenching layers. The data are fitted using the diffusion model used for the $CH_3NH_3PbI_{3-x}Cl_x$ films.

the best values ever reported for small-area (≤ 0.1 cm^2) and large-area (≥ 1 cm^2) perovskite solar cells. Our study sheds light on the importance of processing conditions for preserving long charge carrier diffusion lengths of the perovskite absorbers and interfacial engineering for achieving efficient charge extraction, providing guidelines towards the fabrication of high-efficiency and large-area perovskite solar cells.

4 Experimental methods

4.1 Materials

Zinc acetate dihydrate (> 98%), methylamine (33% in absolute ethanol) and poly(methylmethacrylate) (PMMA) were purchased from Sigma-Aldrich. PbI$_2$ (99.9985%), PbCl$_2$ (99.999%), tetramethylammonium hydroxide (TMAH) (98%), hydroiodic acid (57% in water) and N,N-dimethylformamide (DMF) (anhydrous, amine free; 99.9%) were purchased from Alfa-Aesar. Dimethyl sulphoxide (DMSO), ethyl acetate and ethanol (HPLC grade) were purchased from J & K Chemicals. PCBM and spiro-OMeTAD were purchased from Solenne and Merck respectively. All materials were used as received.

To obtain the CH$_3$NH$_3$PbI$_{3-x}$Cl$_x$ precursor solution, CH$_3$NH$_3$I, synthesized according to reported procedures [10], and PbCl$_2$ were dissolved in DMF with a molar ratio of 3:1. The mixture was stirred at 60 °C overnight in a glovebox. The precursor solution was filtered through polytetrafluoroethylene (PTFE) filters (0.45 μm) before use.

Colloidal ZnO nanocrystals were synthesized by a solution-precipitation process according to literature procedures [41]. Details of synthesis of ZnO nanocrystal and CH$_3$NH$_3$I are provided in the ESM.

4.2 Perovskite films for optical measurements

The CH$_3$NH$_3$PbI$_{3-x}$Cl$_x$ films were deposited by spin-coating the precursor solution (40 wt.%) on pre-cleaned glass substrates at 5,000 rpm for 30 s. After drying at room temperature for ~10 min, the perovskite films were annealed on a hot plate at 95 °C for ~15 min. For post-deposition thermal treatment, the CH$_3$NH$_3$PbI$_{3-x}$Cl$_x$ films were further annealed at different temperatures for the desired durations. All procedures were carried out in a glovebox.

To prepare the CH$_3$NH$_3$PbI$_3$ films, a PbI$_2$ solution (460 mg/mL in DMF) was spin coated on glass substrates at 3,000 rpm for 15 s. Then the substrates were dipped into a CH$_3$NH$_3$I solution (10 mg/mL in 2-propanol) for 60 s, rinsed by 2-propanol and dried at room temperature in air for 5 min.

For optical measurements, the perovskite films were sealed by top layers deposited via spin-coating chlorobenzene solutions of PMMA (10 mg/mL), spiro-OMeTAD (100 mg/mL) or PCBM (30 mg/mL) at 1,500 rpm for 1 min. This procedure was carried out in a glovebox.

4.3 Device fabrication

Solar cell devices were fabricated on patterned ITO coated glass substrates with a sheet resistance of ~20 Ω·sq^{-1}. The substrates were cleaned with acetone, ethanol, and deionized water for 20 min each, followed by UV–ozone treatment for 15 min. PEDOT:PSS (CLEVIOS AL 4083) layers were spin-coated onto the substrates at 4,000 rpm for 60 s and then baked at 120 °C for 20 min in air. The PEDOT:PSS coated substrates were transferred into a glovebox. The CH$_3$NH$_3$PbI$_{3-x}$Cl$_x$ precursor solution was spin-coated at 3,000 rpm for 30 s. After drying at room temperature for ~10 min, the perovskite films were annealed on a hot plate at 95 °C for ~20 min, allowing the color of the films to change to dark brown. The PCBM layers were deposited from a 30 mg/mL chlorobenzene solution at 2,000 rpm for 45 s. Next the ZnO layers were formed by spin-coating a colloidal ZnO nanocrystal solution (8 mg/mL in ethanol) at 3,000 rpm for 45 s. Finally, 150 nm aluminum electrodes were deposited using a thermal evaporation system (Mini SPECTRO, Kurt J. Lesker Co.) through a shadow mask under a high vacuum of ~6 × 10^{-7} Torr. The device area was either 7.25 mm^2 or 1 cm^2 as defined by the overlapping area of the ITO and Al electrodes.

Acknowledgements

Electronic Supplementary Material: Supplementary material (details of the synthesis of ZnO nanocrystals and CH_3NH_3I, the method to fit the charge carrier diffusion lengths, characterization techniques, further information about the interface contacts and device performance) is available in the online version of this article at http://dx.doi.org/10.1007/s12274-014-0534-8.

References

[1] Graetzel, M.; Janssen, R. A. J.; Mitzi, D. B.; Sargent, E. H. Materials interface engineering for solution-processed photovoltaics. *Nature* **2012**, *488*, 304–312.

[2] Halls, J. J. M.; Walsh, C. A.; Greenham, N. C.; Marseglia, E. A.; Friend, R. H.; Moratti, S. C.; Holmes, A. B. Efficient photodiodes from interpenetrating polymer networks. *Nature* **1995**, *376*, 498–500.

[3] Mikhnenko, O. V.; Azimi, H.; Scharber, M.; Morana, M.; Blom, P. W. M.; Loi, M. A. Exciton diffusion length in narrow bandgap polymers. *Energy Environ. Sci.* **2012**, *5*, 6960–6965.

[4] Johnston, K. W.; Pattantyus-Abraham, A. G.; Clifford, J. P.; Myrskog, S. H.; Hoogland, S.; Shukla, H.; Klem, E. J. D.; Levina, L.; Sargent, E. H. Efficient Schottky-quantum-dot photovoltaics: The roles of depletion, drift, and diffusion. *Appl. Phys. Lett.* **2008**, *92*, 122111.

[5] Yu, G.; Gao, J.; Hummelen, J. C.; Wudl, F.; Heeger, A. J. Polymer photovoltaic cells: Enhanced efficiencies via a network of internal donor–acceptor heterojunctions. *Science* **1995**, *270*, 1789–1791.

[6] O'Regan, B.; Grätzel, M. A low-cost, high-efficiency solar cell based on dye-sensitized colloidal TiO_2 films. *Nature* **1991**, *353*, 737–740.

[7] Jean, J.; Chang, S.; Brown, P. R.; Cheng, J. J.; Rekemeyer, P. H.; Bawendi, M. G.; Gradečak, S.; Bulović, V. ZnO nanowire arrays for enhanced photocurrent in PbS quantum dot solar cells. *Adv. Mater.* **2013**, *25*, 2790–2796.

[8] Im, J. H.; Lee, C. R.; Lee, J. W.; Park, S. W.; Park, N. G. 6.5% efficient perovskite quantum-dot-sensitized solar cell. *Nanoscale* **2011**, *3*, 4088–4093.

[9] Kojima, A.; Teshima, K.; Shirai, Y.; Miyasaka, T. Organometal halide perovskites as visible-light sensitizers for photovoltaic cells. *J. Am. Chem. Soc.* **2009**, *131*, 6050–6051.

[10] Lee, M. M.; Teuscher, J.; Miyasaka, T.; Murakami, T. N.; Snaith, H. J. Efficient hybrid solar cells based on meso-superstructured organometal halide perovskites. *Science* **2012**, *338*, 643–647.

[11] Kim, H. S.; Lee, C. R.; Im, J. H.; Lee, K. B.; Moehl, T.; Marchioro, A.; Moon, S. J.; Humphry-Baker, R.; Yum, J. H.; Moser, J. E. et al. Lead iodide perovskite sensitized all-solid-state submicron thin film mesoscopic solar cell with efficiency exceeding 9%. *Sci. Rep.* **2012**, *2*, 591.

[12] Stranks, S. D.; Eperon, G. E.; Grancini, G.; Menelaou, C.; Alcocer, M. J. P.; Leijtens, T.; Herz, L. M.; Petrozza, A.; Snaith, H. J. Electron–hole diffusion lengths exceeding 1 micrometer in an organometal trihalide perovskite absorber. *Science* **2013**, *342*, 341–344.

[13] Xing, G.; Mathews, N.; Sun, S.; Lim, S. S.; Lam, Y. M.; Grätzel, M.; Mhaisalkar, S.; Sum, T. C. Long-range balanced electron- and hole-transport lengths in organic-inorganic $CH_3NH_3PbI_3$. *Science* **2013**, *342*, 344–347.

[14] Burschka, J.; Pellet, N.; Moon, S.-J.; Humphry-Baker, R.; Gao, P.; Nazeeruddin, M. K.; Gratzel, M. Sequential deposition as a route to high-performance perovskite-sensitized solar cells. *Nature* **2013**, *499*, 316–319.

[15] Heo, J. H.; Im, S. H.; Noh, J. H.; Mandal, T. N.; Lim, C. S.; Chang, J. A.; Lee, Y. H.; Kim, H. j.; Sarkar, A.; NazeeruddinMd, K. et al. Efficient inorganic–organic hybrid heterojunction solar cells containing perovskite compound and polymeric hole conductors. *Nat. Photon.* **2013**, *7*, 486–491.

[16] Ball, J. M.; Lee, M. M.; Hey, A.; Snaith, H. J. Low-temperature processed meso-superstructured to thin-film perovskite solar cells. *Energy Environ. Sci.* **2013**, *6*, 1739–1743.

[17] Kim, H. S.; Lee, J. W.; Yantara, N.; Boix, P. P.; Kulkarni, S. A.; Mhaisalkar, S.; Grätzel, M.; Park, N.-G. High efficiency solid-state sensitized solar cell-based on submicrometer rutile TiO_2 nanorod and $CH_3NH_3PbI_3$ perovskite sensitizer. *Nano Lett.* **2013**, *13*, 2412–2417.

[18] Zhang, W.; Saliba, M.; Stranks, S. D.; Sun, Y.; Shi, X.; Wiesner, U.; Snaith, H. J. Enhancement of perovskite-based solar cells employing core–shell metal nanoparticles. *Nano Lett.* **2013**, *13*, 4505–4510.

[19] Abrusci, A.; Stranks, S. D.; Docampo, P.; Yip, H.-L.; Jen, A. K.-Y.; Snaith, H. J. High-performance perovskite–polymer hybrid solar cells via electronic coupling with fullerene monolayers. *Nano Lett.* **2013**, *13*, 3124–3128.

[20] Etgar, L.; Gao, P.; Xue, Z.; Peng, Q.; Chandiran, A. K.; Liu, B.; Nazeeruddin, M. K.; Grätzel, M. Mesoscopic CH₃NH₃PbI₃/TiO₂ heterojunction solar cells. *J. Am. Chem. Soc.* **2012**, *134*, 17396–17399.

[21] Kumar, M. H.; Yantara, N.; Dharani, S.; Graetzel, M.; Mhaisalkar, S.; Boix, P. P.; Mathews, N. Flexible, low-temperature, solution processed ZnO-based perovskite solid state solar cells. *Chem. Commun.* **2013**, *49*, 11089–11091.

[22] Wojciechowski, K.; Saliba, M.; Leijtens, T.; Abate, A.; Snaith, H. J. Sub 150 °C orocessed meso-superstructured perovskite solar cells with enhanced efficiency. *Energy Environ. Sci.* **2013**, *7*, 1142–1147.

[23] Chen, Q.; Zhou, H.; Hong, Z.; Luo, S.; Duan, H.-S.; Wang, H. H.; Liu, Y.; Li, G.; Yang, Y. Planar heterojunction perovskite solar cells via vapor-assisted solution process. *J. Am. Chem. Soc.* **2014**, *136*, 622–625.

[24] Liu, D.; Kelly, T. L. Perovskite solar cells with a planar heterojunction structure prepared using room-temperature solution processing techniques. *Nat. Photon.* **2014**, *8*, 133–138.

[25] Malinkiewicz, O.; Yella, A.; Lee, Y. H.; Espallargas, G. M.; Graetzel, M.; Nazeeruddin, M. K.; Bolink, H. J. Perovskite solar cells employing organic charge-transport layers. *Nat. Photon.* **2014**, *8*, 128–132.

[26] Jeng, J.-Y.; Chiang, Y.-F.; Lee, M.-H.; Peng, S.-R.; Guo, T.-F.; Chen, P.; Wen, T.-C. CH₃NH₃PbI₃ perovskite/fullerene planar-heterojunction hybrid solar cells. *Adv. Mater.* **2013**, *25*, 3727–3732.

[27] Eperon, G. E.; Burlakov, V. M.; Docampo, P.; Goriely, A.; Snaith, H. J. Morphological control for high performance, solution-processed planar heterojunction perovskite solar cells. *Adv. Funct. Mater.* **2014**, *24*, 151–157.

[28] You, J.; Hong, Z.; Yang, Y.; Chen, Q.; Cai, M.; Song, T.-B.; Chen, C.-C.; Lu, S.; Liu, Y.; Zhou, H. et al. Low-temperature solution-processed perovskite solar cells with high efficiency and flexibility. *ACS Nano* **2014**, *8*, 1674–1680.

[29] Sun, S.; Salim, T.; Mathews, N.; Duchamp, M.; Boothroyd, C.; Xing, G.; Sum, T. C.; Lam, Y. M. The origin of high efficiency in low-temperature solution-processable bilayer organometal halide hybrid solar cells. *Energy Environ. Sci.* **2014**, *7*, 399–407.

[30] Docampo, P.; Ball, J. M.; Darwich, M.; Eperon, G. E.; Snaith, H. J. Efficient organometal trihalide perovskite planar-heterojunction solar cells on flexible polymer substrates. *Nat. Commun.* **2013**, *4*, 2761.

[31] Liu, M.; Johnston, M. B.; Snaith, H. J. Efficient planar heterojunction perovskite solar cells by vapour deposition. *Nature* **2013**, *501*, 395–398.

[32] Conings, B.; Baeten, L.; De Dobbelaere, C.; D'Haen, J.; Manca, J.; Boyen, H.-G. Perovskite-based hybrid solar cells exceeding 10% efficiency with high reproducibility using a thin film sandwich approach. *Adv. Mater.* **2014**, *26*, 2041–2046.

[33] Eperon, G. E.; Stranks, S. D.; Menelaou, C.; Johnston, M. B.; Herz, L. M.; Snaith, H. J. Formamidinium lead trihalide: A broadly tunable perovskite for efficient planar heterojunction solar cells. *Energy Environ. Sci.* **2014**, *7*, 982–988.

[34] Cheng, Z.; Lin, J. Layered organic–inorganic hybrid perovskites: Structure, optical properties, film preparation, patterning and templating engineering. *Cryst. Eng. Comm* **2010**, *12*, 2646–2662.

[35] Noh, J. H.; Im, S. H.; Heo, J. H.; Mandal, T. N.; Seok, S. I. Chemical management for colorful, efficient, and stable inorganic–organic hybrid nanostructured solar cells. *Nano Lett.* **2013**, *13*, 1764–1769.

[36] Dualeh, A.; Tétreault, N.; Moehl, T.; Gao, P.; Nazeeruddin, M. K.; Grätzel, M. Effect of annealing temperature on film morphology of organic–inorganic hybrid pervoskite solid-state solar cells. *Adv. Funct. Mater.* **2014**, *24*, 3250–3258.

[37] Snaith, H. J.; Abate, A.; Ball, J. M.; Eperon, G. E.; Leijtens, T.; Noel, N. K.; Stranks, S. D.; Wang, J. T.-W.; Wojciechowski, K.; Zhang, W. Anomalous hysteresis in perovskite solar cells. *J. Phys. Chem. Lett.* **2014**, *5*, 1511–1515.

[38] Jørgensen, M.; Norrman, K.; Krebs, F. C. Stability/ degradation of polymer solar cells. *Sol. Energy Mater. Sol. Cells* **2008**, *92*, 686–714.

[39] Wang, M.; Xie, F.; Du, J.; Tang, Q.; Zheng, S.; Miao, Q.; Chen, J.; Zhao, N.; Xu, J. B. Degradation mechanism of organic solar cells with aluminum cathode. *Sol. Energy Mater. Sol. Cells* **2011**, *95*, 3303–3310.

[40] Zhang, Q.; Wan, X.; Xing, F.; Huang, L.; Long, G.; Yi, N.; Ni, W.; Liu, Z.; Tian, J.; Chen, Y. Solution-processable graphene mesh transparent electrodes for organic solar cells. *Nano Res.* **2013**, *6*, 478–484.

[41] Schwartz, D. A.; Norberg, N. S.; Nguyen, Q. P.; Parker, J. M.; Gamelin, D. R. Magnetic quantum dots: Synthesis, spectroscopy, and magnetism of Co²⁺- and Ni²⁺- doped ZnO nanocrystals. *J. Am. Chem. Soc.* **2003**, *125*, 13205–13218.

[42] Yin, X.; Wang, B.; He, M.; He, T. Facile synthesis of ZnO nanocrystals via a solid state reaction for high performance plastic dye-sensitized solar cells. *Nano Res.* **2012**, *5*, 1–10.

[43] Krebs, F. C.; Spanggard, H.; Kjær, T.; Biancardo, M.; Alstrup, J. Large area plastic solar cell modules. *Mater. Sci. Eng. B* **2007**, *138*, 106–111.